

INTRODUCTION

Above Earth's atmosphere are the Van Allen radiation belts, a toroidally-shaped pair of belts that consist of a complex and dynamic plasma environment. The inner radiation belt is stable, consists of mostly energetic protons, and is located within 2 Earth radii (measured near the equator) above Earth's surface. The outer radiation belt, on the other hand, consists of mostly energetic electrons, is dynamic on hour time scales, and is typically found between three and eight Earth radii above Earth's surface. These belts pose a threat to space exploration due to their adverse effects on our bodies and electrical components. A few effects include: a high radiation dose for manned missions, degradation of silicon that causes transistor malfunction, computer memory corruption due to bit flips, etc. With these effects in mind, it is no surprise that the radiation belts have been extensively studied since their discovery in the 1960s.

The radiation belt particles, mostly consisting of electrons and protons, are at times unstable to wave growth and generate electric and magnetic waves. These waves can then accelerate and scatter radiation belt particles with a variety of wave-particle mechanisms. These wave-particle interactions are believed to be responsible for scattering electron microbursts—a short and intense increase of precipitating electrons into Earth's atmosphere—that are capable of destroying ozone molecules and rapidly deplete the outer belt's electrons.

Electron microbursts, henceforth referred to as microbursts, are typically observed by low Earth orbiting spacecraft, sounding rockets, and high altitude balloons as a sub-second impulse of electrons. Some of the most intense microbursts have electron fluxes that are a factor of 10 to 100 above the background (for example see Fig. 7 in Blake et al. (1996)). Since they were first reported by Anderson and

Milton (1964), the intense transient nature of microbursts have compelled researchers to pursue an understanding of their properties, their effects on the environment, and the physical mechanism(s) that create microbursts. Microbursts are widely believed to be created by wave-particle scattering between a plasma wave called whistler mode chorus and outer radiation belt electrons, although many details regarding the scattering mechanism are unconstrained or unknown. The goal of this dissertation is to expand our knowledge of the wave-particle scattering mechanism that causes electron microbursts.

This chapter serves as an introduction to the fundamental physical concepts that are essential to understand wave-particle interactions in Earth's magnetosphere. We will review the main structures in the magnetosphere, the motion of charged particles in electric and magnetic fields, how particles are accelerated and lost in the magnetosphere, and asses the current state of our understanding of microbursts.

Then the rest of this dissertation expands our knowledge of microbursts. In Chapter ?? (chapter numbers will be filled in the full dissertation) we will investigate and model the scattering mechanism responsible for microbursts observed inside the outer radiation belt, near the magnetic equator. Then in Chapters ?? and ?? we will investigate the microburst scattering mechanism indirectly by estimating the microburst footprint size in low Earth orbit and the magnetic equator (near where microburst electrons are believed to be scattered) and compare it to sizes of chorus waves estimated in prior literature.

Particle Populations and Their Interractions in the Magnetosphere

To set the scene, we will briefly tour the various populations in the magnetosphere that are most relevant to this dissertation, and are illustrated in Fig. 1.1.

The sun and its solar wind are ultimately the source of energy input into the

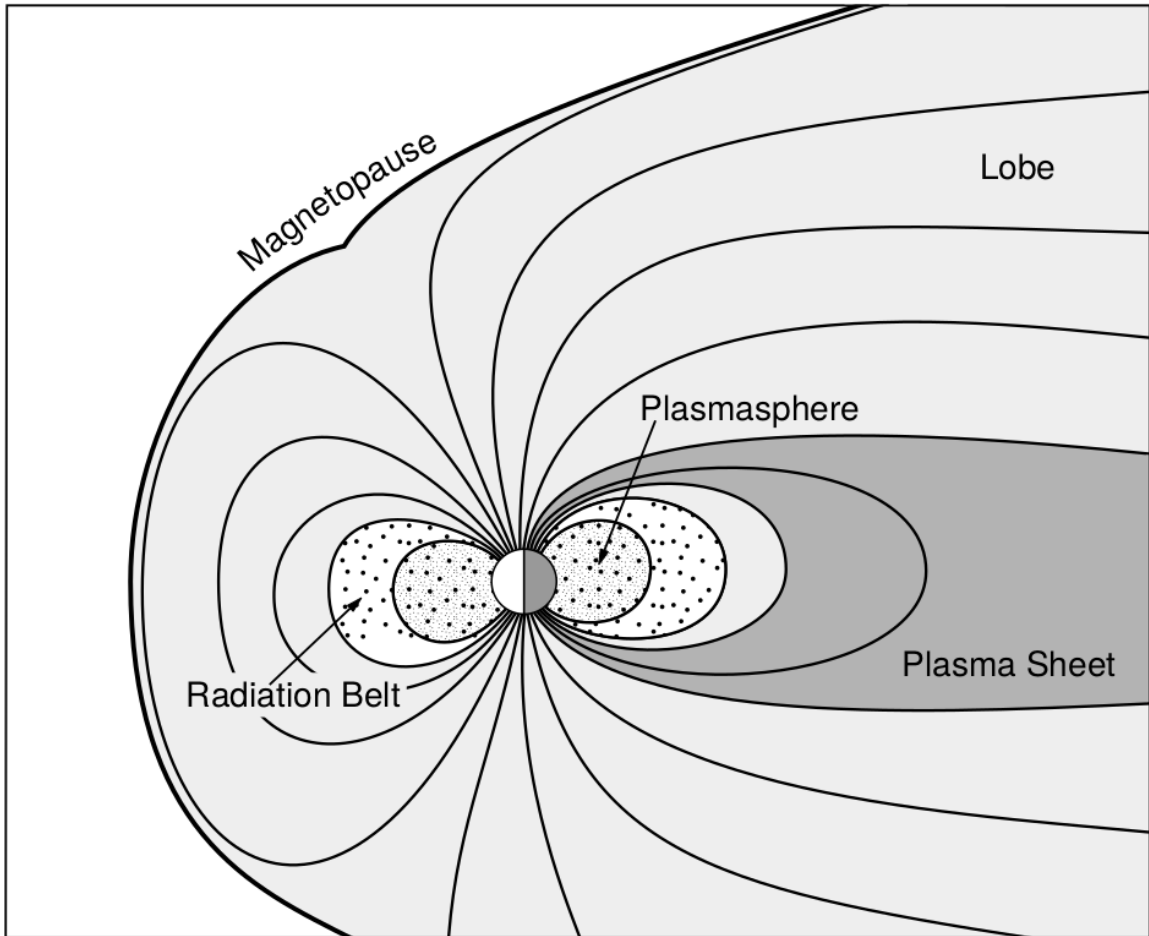


Figure 1.1: A few macroscopic structures in the magnetosphere. The magnetosphere boundary with the solar wind is the magnetopause. The magnetotail consists of two lobes that contain Earth's magnetic flux with the plasma sheet separating the two lobes. The inner magnetosphere contains the plasmasphere, the ring current, and the radiation belts which are co-located. Figure from Baumjohann and Treumann (1997).

magnetosphere. The solar wind at Earth's orbit is a plasma traveling at supersonic speeds with an embedded interplanetary magnetic field (IMF). When the solar wind encounters Earth's magnetic field, the plasma can not easily penetrate into the magnetosphere because the solar wind plasma is frozen-in to the IMF. The frozen-in property is a direct consequence of the solar wind's nearly infinite conductivity. Thus the plasma and its magnetic field drapes around the magnetosphere, forming a cavity in the solar wind that qualitatively has a shape similar to in Fig. 1.1. The solar wind is supersonic at 1 AU so a bow shock exists upstream of the magnetosphere which compresses and heats the solar wind. Downstream of the bow shock, the solar wind plasma flows around the magnetosphere inside the magnetosheath. The magnetopause is the surface where the solar wind ram and Earth's magnetic pressures balance. To first order, the magnetopause can be thought of as a boundary between the solar wind and Earth's magnetosphere. The shocked plasma then flows past the Earth where it shapes the magnetotail. In the magnetotail, the magnetopause exists where the solar wind magnetic pressure balances Earth's magnetic field pressure in the lobes. The magnetotail extends on the order of $100 R_E$ downstream of Earth, and the tailward stretching of magnetic field lines creates a region where Earth's earthward and anti-earthward magnetic fields are in proximity. In this region, the curl of \vec{B} is non-zero, thus by Ampere's law there must be a current (called the plasma sheet) near the magnetic equator (e.g. ?).

Populations in the Inner Magnetosphere

Closer to Earth, where the magnetic field is largely dipolar, are three plasma populations that comprise the inner magnetosphere: the plasmasphere, the ring current, and the radiation belts which are shown in Fig. 1.1. Before we describe these three particle populations in detail, we will introduce the coordinate system

that most naturally describes the inner magnetosphere environment, and the electric fields that mostly effect low energy particles.

This coordinate system is shown in Fig. 1.2 and it naturally describes particles in a dipole magnetic field geometry. In this coordinate system the “radial” coordinate is the L shell. The L -shell (L) is the distance from the Earth’s center to the location where a particular magnetic field line crosses the magnetic equator, in units of Earth radii, $R_e = 6,371$ km. The azimuthal coordinate is the magnetic local time (MLT). For an observer above Earth’s north pole looking down, MLT is defined to be 0 (midnight) in the anti-sunward direction and increases in the counter-clockwise direction with 6 at dawn, 12 at noon (sunward direction), and 18 at dusk. The final coordinate is the magnetic latitude, λ , which is analogous to the latitude coordinate in the spherical coordinate system and is defined to be 0 at the magnetic equator. This coordinate system naturally describes the inner magnetosphere populations described below.

Low energy particle dynamics in the inner magnetosphere are driven by the co-rotation and the dawn-dusk (pointing from approximately 6 to 18 MLT) electric fields. The co-rotation electric field arises from Earth’s rotation. Earth’s magnetic field and the particles frozen on it rotate with the Earth so in the magnetosphere (non-rotating) reference frame the particles appear to $\vec{E} \times \vec{B}$ drift (which will be described in the next section) with Earth’s rotation. The co-rotation \vec{E} points towards Earth. The convection electric field points from dawn to dusk, and is due to the Earthward transport of particles from the magnetotail. The superposition of the co-rotation and convection electric fields is a potential field shown in Fig. 1.3. The shaded area in Fig. 1.3 shows where low energy electrons execute closed orbits around Earth (i.e. particles are trapped), and outside this region the electrons are not trapped. The dynamic topology of the shaded region in Fig. 1.3 is controlled by only the convection

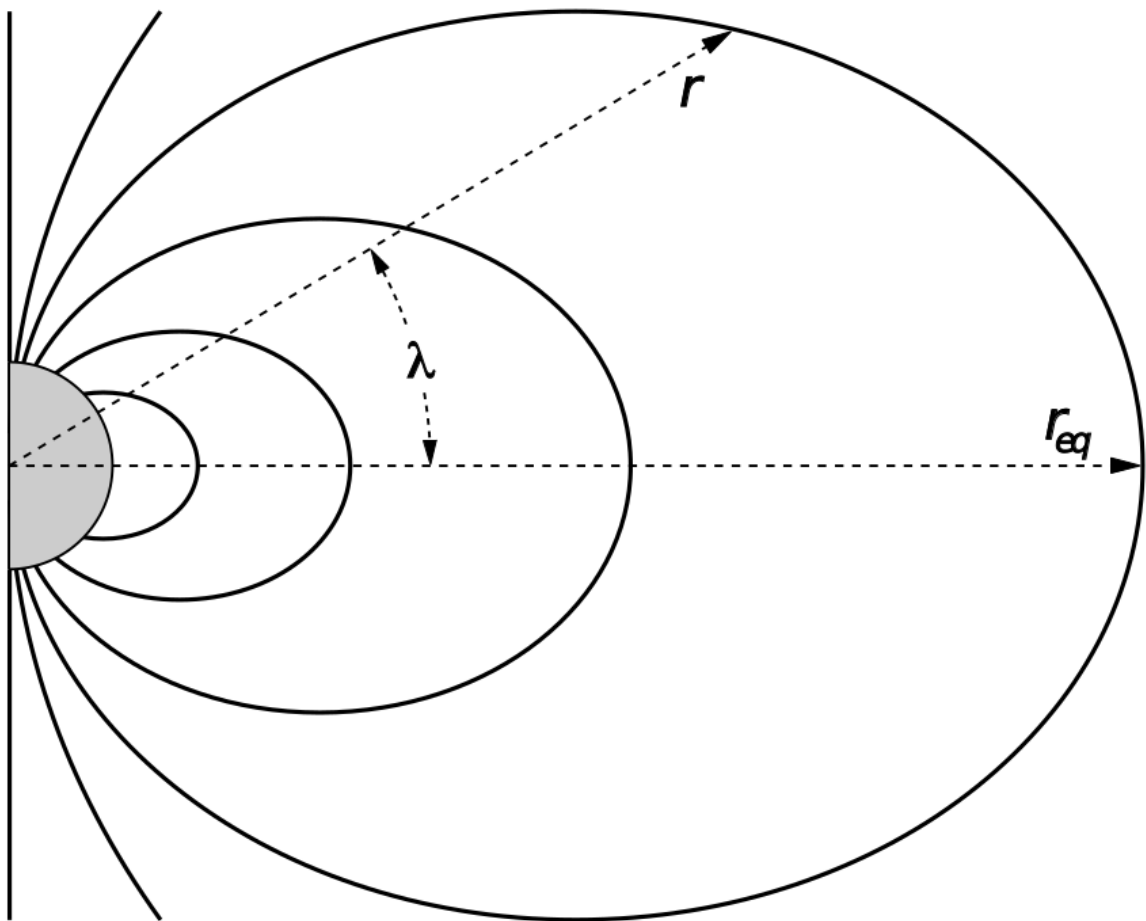


Figure 1.2: The dipole coordinate system. The magnetic latitude of \mathbf{r} is λ . The radial distance to a magnetic field line in the equatorial plane is typically given by $L = r_{eq}/R_e$. Figure from Baumjohann and Treumann (1997).

electric field which is dependent on the solar wind speed and the IMF. The lowest energy particles that orbit along equipotential lines in the shaded region in Fig. 1.3 make up the plasmasphere.

Plasmasphere The plasmasphere is a relatively dense ($n_e \sim 10^3/\text{cm}^3$) and cool ($\sim \text{eV}$) plasma. The plasmasphere typically extends to $L \sim 4$ and the spatial extent is highly dependent on the solar wind and magnetospheric conditions. The source of the plasmasphere is the ionosphere, a layer in Earth's upper atmosphere that contains a high concentration of electrons and ions. The main mechanisms that ionize the ionosphere are ultraviolet light from the sun and particle precipitation. The ultraviolet ionization by sunlight is strongly dependent on the time of day and latitude, while particle precipitation is highly dependent on magnetospheric conditions and mostly occurs at high latitudes.

The outer boundary of the plasmasphere is called the plasmapause which is typically identified by a steep radial gradient in plasma density from $\sim 10^3/\text{cm}^3$ to $\sim 1/\text{cm}^3$. It is important to know the location of the plasmapause since the plasma density strongly controls the efficiency of particle scattering by waves. For example, electron scattering by chorus waves is more efficient when the ratio of the plasma and gyro frequency is low which is typically found in low plasma density regions outside of the plasmapause (e.g. Horne et al., 2005; O'Brien and Moldwin, 2003; ?).

Ring Current A higher energy population is the ring current. This population consists of protons and electrons between tens and a few hundred keV that drift around the Earth. The orbits of higher energy particles are not as affected by the convection and co-rotation electric field, instead they drift around the Earth due to gradient and curvature drifts which will be described in the following section. Since the direction of the drift is dependent on charge, protons drift west around the Earth

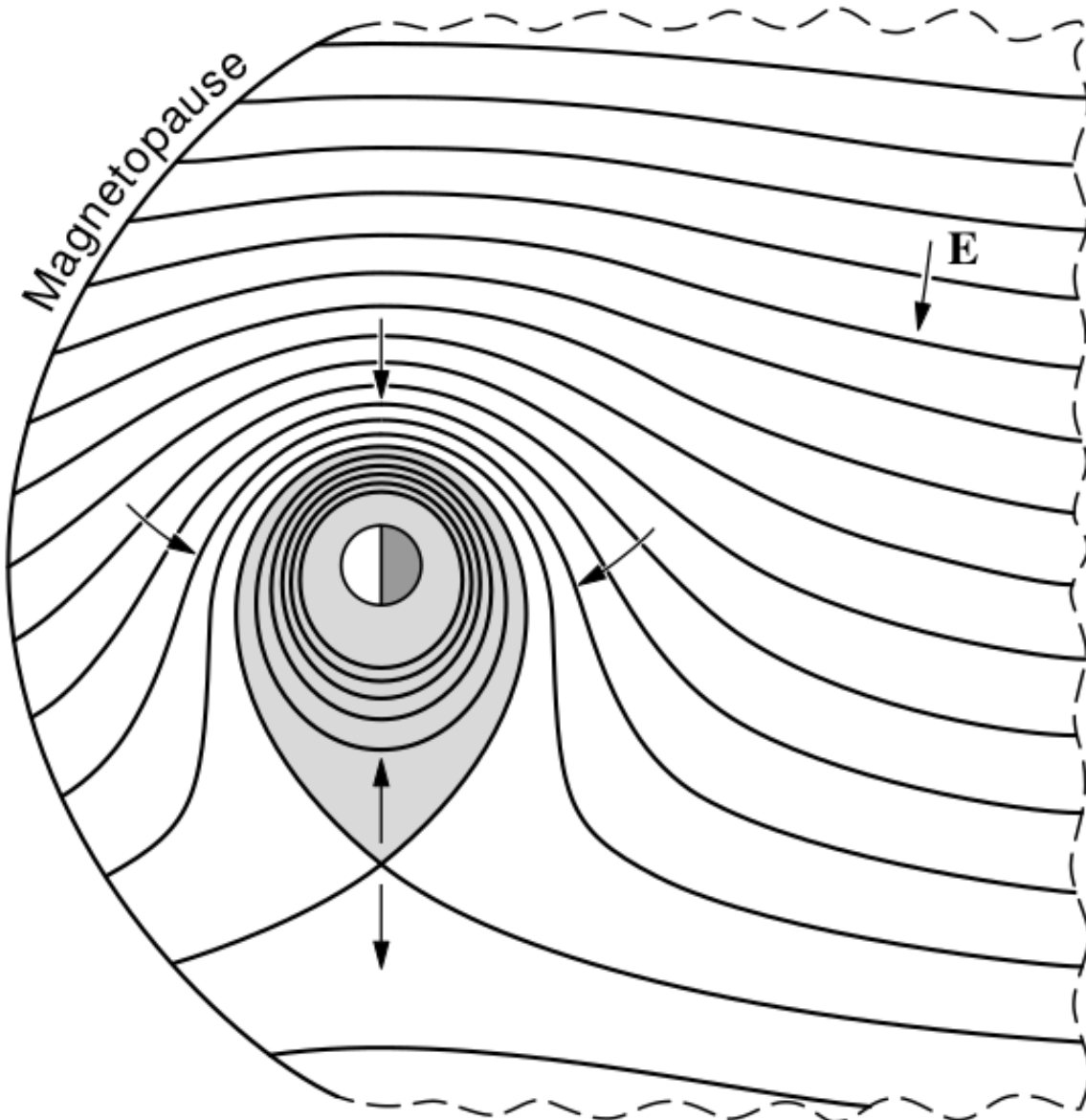


Figure 1.3: Equipotential lines and electric field arrows due to the superposition of the co-rotation and convection electric fields. The trajectories of low energy electrons follow these equipotential lines. In the shaded region the low energy electrons execute closed orbits, while outside they follow trajectories that go through the magnetopause. The region separating the two regimes is called the Alfvén layer. Figure from Baumjohann and Treumann (1997).

and electrons drift East. This effect creates a current around the Earth.

The ring current generates a magnetic field which decreases the magnetic field strength at the surface of the Earth and increases it outside of the ring current. The decrease of Earth's magnetic field strength is readily observed by a system of ground-based magnetometers and is merged into a Disturbance Storm Time (DST) index to quantify the global reduction in the magnetic field. An example of a DST index time series from the 2015 St. Patrick's Day storm, driven by a coronal mass ejection (CME), is shown in Fig. 1.4. At the start of a storm, DST sometimes increases in response to the compression of the magnetopause by a shock wave (termed the initial phase or sudden storm commencement) and is shown by the red horizontal bar in Fig. 1.4. During the main phase of the storm the ring current population is rapidly built up and DST rapidly decreases which is shown by the green bar in Fig. 1.4. After the storm is over, the ring current slowly recovers to pre-storm conditions during the recovery phase shown by the blue bar in Fig. 1.4. In the recovery phase, the ring current gradually decays due to particles losses into the atmosphere, or transport through the magnetopause via mechanisms described later in this chapter. The DST index, along with other geomagnetic indices, are used by the space physics community to quantify the global state of the magnetosphere.

Radiation Belts The highest particle energy populations are in the Van Allen radiation belts. These belts were discovered by Van Allen (1959) and Vernov and Chudakov (1960) during the Cold War and are a pair of toroidally shaped populations of trapped electrons and protons shown in Fig. 1.5. Their quiescent toroidal shape, similar to the shape of the plasmasphere and ring current, is a result of Earth's dipole magnetic field.

The inner radiation belt is extremely stable on year time periods, extends to

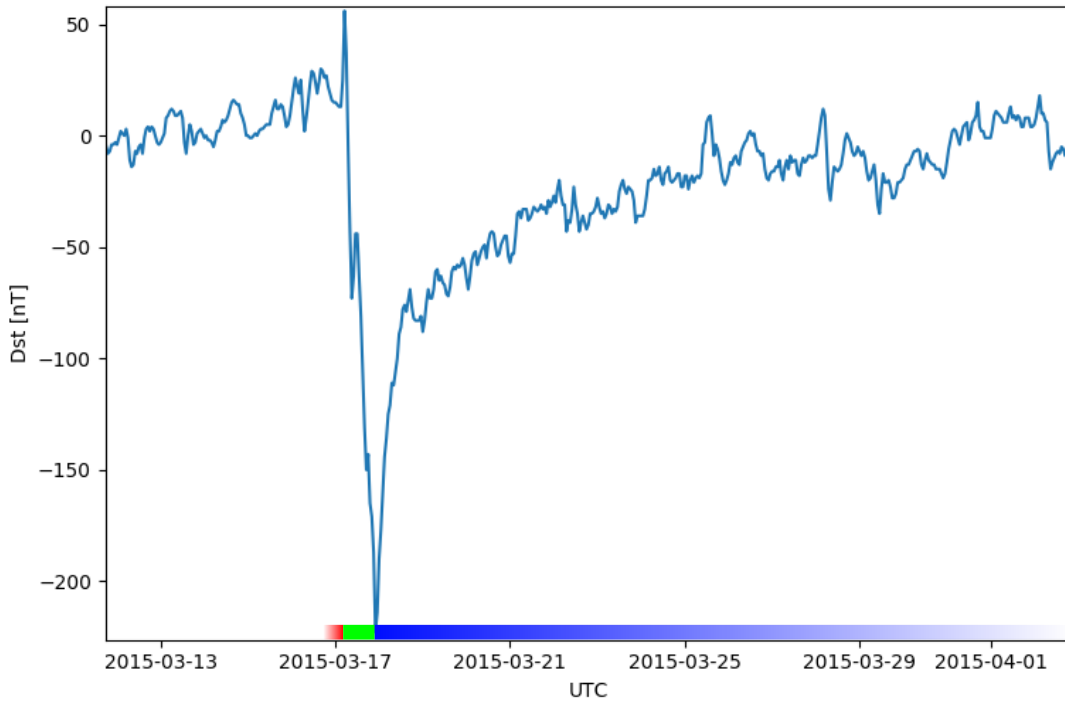


Figure 1.4: The DST index during the St. Patrick's Day 2015 storm. This storm was caused by a coronal mass ejection on March 15th, 2015. The storm phases are: initial phase, main phase, and recovery phase. The initial phase occurred when the Dst peaked at $+50$ nT on March 17th during which the ring current was eroded by the coronal mass ejection during the interval shown by the red bar shown at the bottom. Then the following rapid decrease to ≈ -200 nT was during the main phase where many injections from the magnetotail enhanced the ring current, which reduced Earth's magnetic field strength at the ground, and is shown with the green bar. Lastly, the recovery phase lasted from March 18th to approximately March 29th during which the ring current particles were lost and the ring current returned to its equilibrium state. The recovery phase is shown with the blue bar.

The Earth's Electron Radiation Belts

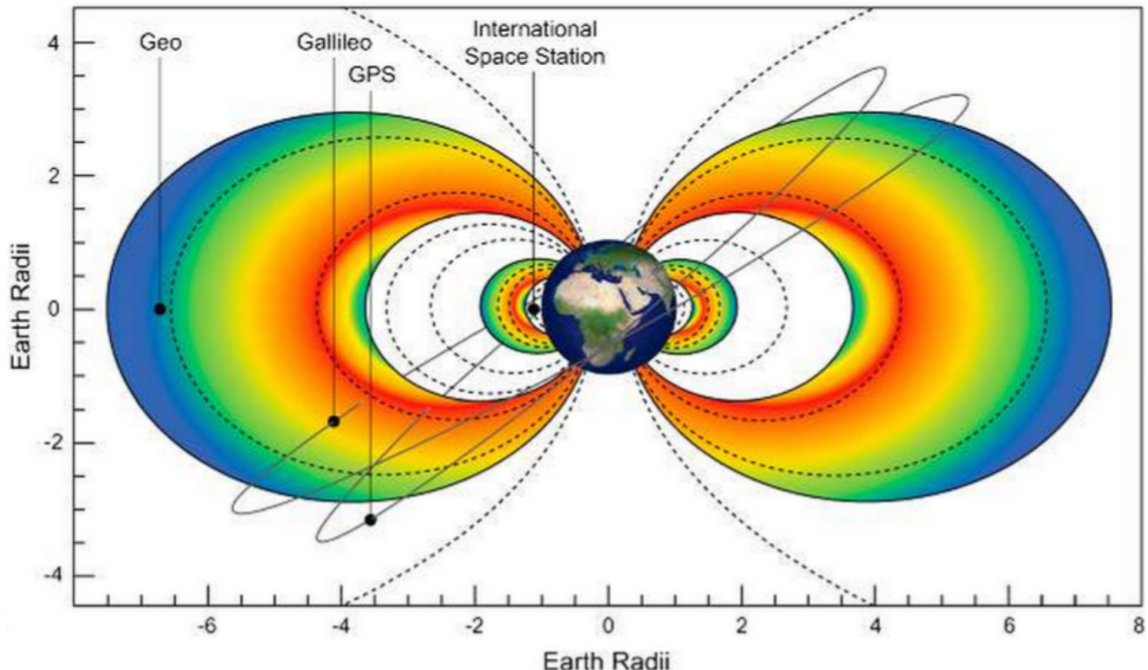


Figure 1.5: The two radiation belts with the locations of various satellites and orbits. Figure from (Horne et al., 2013).

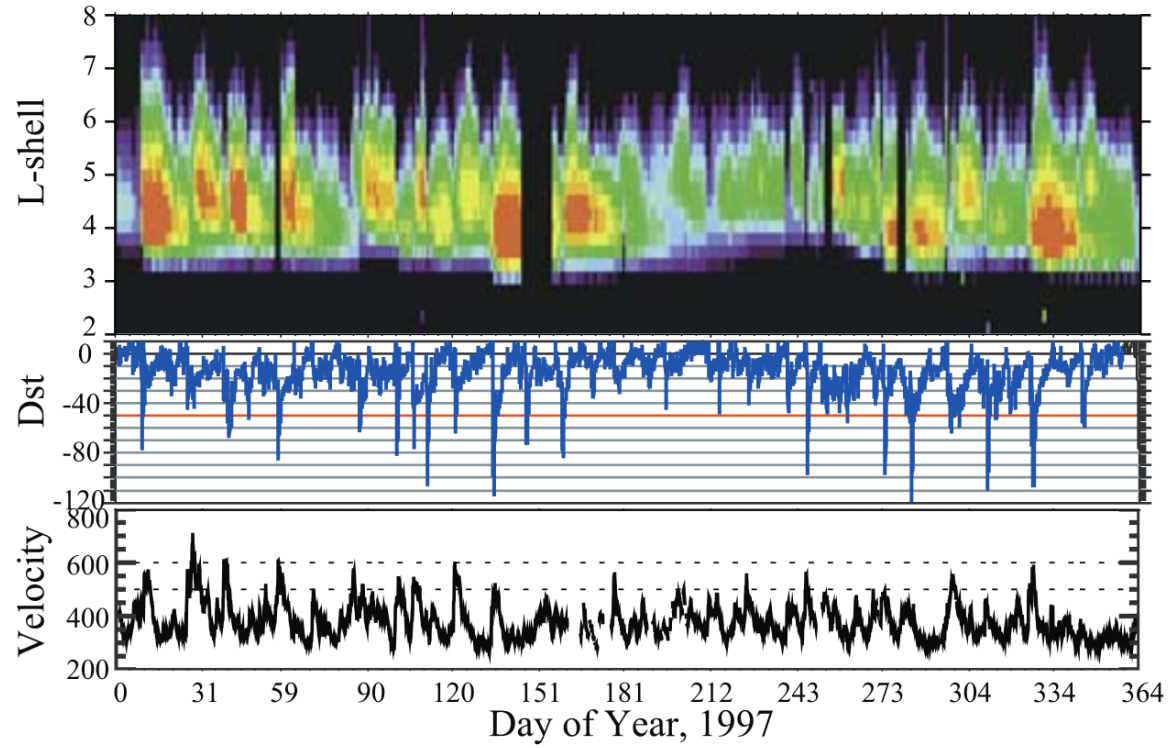


Figure 1.6: The dynamics of the outer radiation belt in 1997 from the POLAR satellite. Top panel shows the 1.2-2.4 MeV electron flux as a function of L and 1997 day of year. The middle panel shows the DST index, and bottom panel shows the solar wind velocity. Figure from (Reeves et al., 2003).

$L \approx 3$, and mainly consists of protons with energies between MeV and GeV and electrons with energies up to ≈ 1 MeV (Claudepierre et al., 2019). The source of inner radiation belt protons is believed to be due to cosmic-ray albedo neutron decay (e.g. Li et al., 2017) and inward radial diffusion for electrons (e.g. O'Brien et al., 2016). The gap between the inner and outer radiation belt is called the slot, which is believed to be due to particle scattering into the atmosphere by hiss waves (e.g. Breneman et al., 2015; Lyons and Thorne, 1973).

The outer radiation belt is much more dynamic and consists of mainly electrons of energies up to a few MeV. The outer belt's spatial extent is highly variable as shown in Fig. 1.6, and is typically observed between L of 4 and 8. The source of outer radiation belt electrons is widely believed to be injections of plasma from the magnetotail that is then accelerated to high energies. This dissertation focuses on understanding electron microburst precipitation from the outer radiation belt which is described below.

Charged Particle Motion in Electric and Magnetic Fields

A charged particle trapped in the magnetosphere will experience three types of periodic motion in Earth's nearly dipolar magnetic field in the absence of electric fields. The three motions are ultimately due to the Lorentz force that a particle of momentum \vec{p} , charge q , and velocity \vec{v} experiences in an electric field \vec{E} and magnetic field \vec{B} and is given by

$$\frac{d\vec{p}}{dt} = q(\vec{E} + \vec{v} \times \vec{B}). \quad (1.1)$$

For many vector quantities in this dissertation, we will adopt a widely-used convention by splitting up vectors into parallel, $x_{||}$, and perpendicular, x_{\perp} components with respect to the background magnetic field. In the magnetosphere, the three

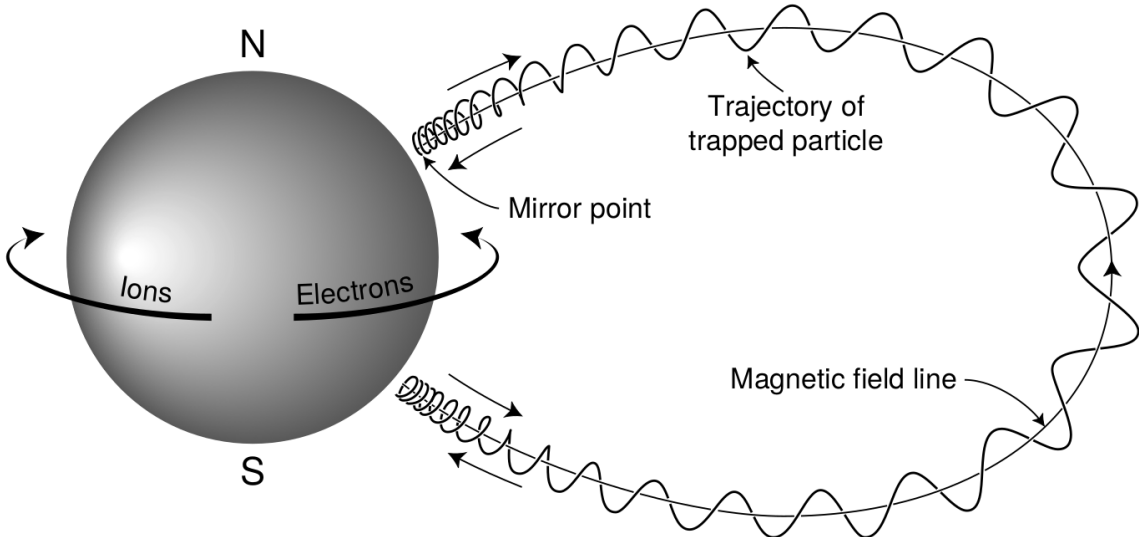


Figure 1.7: The three periodic motions of charged particles in Earth's dipole magnetic field. These motions are: gyration about the magnetic field line, bounce motion between the magnetic poles, and azimuthal drift around the Earth. Figure from (Baumjohann and Treumann, 1997).

periodic motions, in decreasing frequency, are gyration, bounce, and drift and are schematically shown in Fig. 1.7. Each periodic motion has a corresponding conserved quantity or adiabatic invariant.

The highest frequency periodic motion is gyration about a magnetic field of magnitude B . This motion is circular with a Larmor radius of

$$r = \frac{mv_{\perp}}{|q|B} \quad (1.2)$$

where m is the mass and v_{\perp} the particle's velocity perpendicular to \vec{B} . This motion has a corresponding gyrofrequency of

$$\Omega = \frac{|q|B}{m} \quad (1.3)$$

in units of radians/second. In the radiation belts, the electron gyrofrequency, Ω_e , is on

the order of a kHz near the magnetic equator. The corresponding adiabatic invariant is found by integrating the particle's canonical momentum around the particle's path of gyration,

$$J_i = \oint (\vec{p} + q\vec{A}) \cdot d\vec{l} \quad (1.4)$$

where J_i is the i^{th} adiabatic invariant and \vec{A} is the magnetic vector potential. This integral is carried out by integrating the first term over the circumference of the gyro orbit and integrating the second term using Stokes theorem to calculate the magnetic flux enclosed by the gyro orbit. The gyration invariant is $J_1 \sim v_{\perp}^2/B$ which is conserved when the frequency, ω , of a force acting on the gyrating electron satisfies $\omega \ll \Omega_e$.

The second highest frequency periodic motion is bouncing due to a parallel gradient in \vec{B} . This periodic motion naturally arises in the magnetosphere because Earth's magnetic field is stronger near the poles. To understand this motion we first need to define the concept of pitch angle, α as the angle between \vec{B} and \vec{v} which is schematically shown in Fig. 1.8a. The pitch angle relates v with v_{\perp} and v_{\parallel} , the component of the particles velocity parallel to \vec{B} . As shown in Fig. 1.8b and 1.8c, a smaller (larger) α will increase (decrease) the distance that the charged particle travels parallel to \vec{B} during one gyration.

Assuming the particle's kinetic energy is conserved, the conservation of J_1 implies that given a particle's $v_{\perp}(0)$ and $B(0)$ at the magnetic equator (where Earth's magnetic field is usually at a minimum) we can calculate its $v_{\perp}(s)$ along the particle's path, s , by calculating $B(s)$ from magnetic field models. Thus the particle's perpendicular velocity is then related via

$$\frac{v_{\perp}^2(0)}{B(0)} = \frac{v_{\perp}^2(s)}{B(s)} \quad (1.5)$$

which can be rewritten as

$$\frac{v^2 \sin^2 \alpha(0)}{B(0)} = \frac{v^2 - v_{||}^2(s)}{B(s)} \quad (1.6)$$

and re-arranged to solve for $v_{||}(s)$ by

$$v_{||}(s) = v \sqrt{1 - \frac{B(s)}{B(0)} \sin^2 \alpha(0)} \quad (1.7)$$

which will tend towards 0 as the second term in the radical approaches 1.

The location where $v_{||}(s) = 0$ is called the mirror point and is where a particle stops and reverses direction. Since Earth's magnetic field is stronger towards both poles, the mirroring particle will execute periodic bounce motion between two mirror points in the northern and southern hemispheres. The corresponding adiabatic invariant, J_2 is

$$J_2 = \oint p_{||} ds \quad (1.8)$$

where ds describes the particle path between the mirror points in the northern and southern hemispheres (see Fig. 1.7). J_2 is found by substituting Eq. 1.7 into Eq. 1.8 and defining the magnetic field strength at the mirror points as B_m (where $\alpha(m) = 90^\circ$). The J_2 integral can be written as

$$J_2 = 2p \int_{m_n}^{m_s} \sqrt{1 - \frac{B(s)}{B(m)}} ds \quad (1.9)$$

where m_n and m_s are the northern and southern mirror points, respectively. The

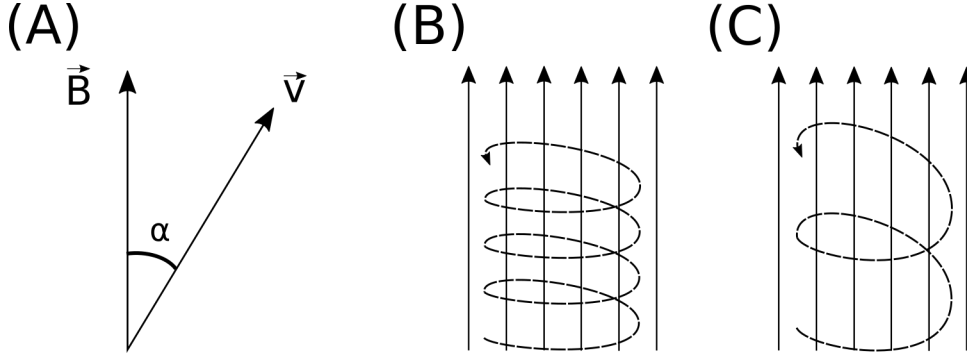


Figure 1.8: Charged particle motion in a uniform magnetic field \vec{B} . Panel (A) shows the geometry defining the pitch angle, α . Panel (B) and (C) show two helical electron trajectories with dashed lines assuming a large and small α (corresponding to a small and large parallel velocity $v_{||}$), respectively.

bounce period can be estimated (e.g. Baumjohann and Treumann, 1997) to be

$$t_b \approx \frac{LR_e}{\sqrt{W/m}}(3.7 - 1.6 \sin \alpha(0)) \quad (1.10)$$

where W is the particle's kinetic energy. As with gyration, the particle will bounce between the mirror points as long as $\omega \ll \Omega_b$, where Ω_b is the bounce frequency.

At this stage it is instructional to introduce loss cone pitch angle, α_L . Conventionally, the loss cone pitch angle is defined as the pitch angle where a particle will mirror at ≈ 100 km altitude in the atmosphere. A charged particle gyrating at those altitudes will encounter, and likely Coulomb scatter, with the dense atmosphere and be lost. The 100 km altitude is only a convention and not a hard boundary, e.g. the peak in the 1 MeV electron ionization rate is at ≈ 60 km altitudes (?).

The slowest periodic motion experienced by charged particles in Earth's magnetic field is azimuthal drift around the Earth. This drift primarily results from a combination of a radial gradient in \vec{B} and the curvature of the magnetic field. The radial gradient drift arises because Earth's magnetic field is stronger near the Earth. The particle's gyroradius shrinks as it gyrates towards Earth, and expands when it

gyrates away from Earth. The overall effect is the particle gyro orbit does not close on itself causing eastward drift of negatively charged particles and westward drift of positively charged particles. The radial gradient drift is further enhanced by the centrifugal force that a particle experiences as it bounces along the curved field lines. The drift adiabatic invariant, J_3 is found by integrating Eq. 1.4 over the complete particle orbit around the Earth. The shape of this drift orbit is known as a drift shell, and can be visualized by rotating the trapped particle trajectory in Fig. 1.7 around the axis that connects the poles. For J_3 , the first term is negligible and the second term is the magnetic flux enclosed by the drift shell, Φ_m i.e. $J_3 \sim \Phi_m$.

To quantify the frequencies of the three periodic motions, Fig. 1.9 from Schulz and Lanzerotti (1974) shows contours of the gyration, bounce, and drift frequencies for electrons and protons in Earth's dipole magnetic field.

Up until now we have considered the three periodic motions due Earth's magnetic field in the absence of electric fields. If there is an electric field, \vec{E} , perpendicular to \vec{B} , a particle's center of gyration (averaged position of the particle over a gyration) will drift with a velocity perpendicular to both \vec{E} and \vec{B} . The drift velocity can be solved using Eq. 1.1 and is

$$\vec{v}_E = \frac{\vec{E} \times \vec{B}}{B^2}. \quad (1.11)$$

If there is a parallel electric field, $E_{||}$, then the particle is accelerated along the magnetic field line. An $E_{||}$ pointing away from the Earth will contribute to the mirror force and raise the particle's mirror point. On the contrary, an Earthward pointing $E_{||}$ will oppose the mirror force and lower the mirror point. If the Earthward $E_{||}$ lowers the mirror point into the atmosphere, those particles will precipitate into the atmosphere.

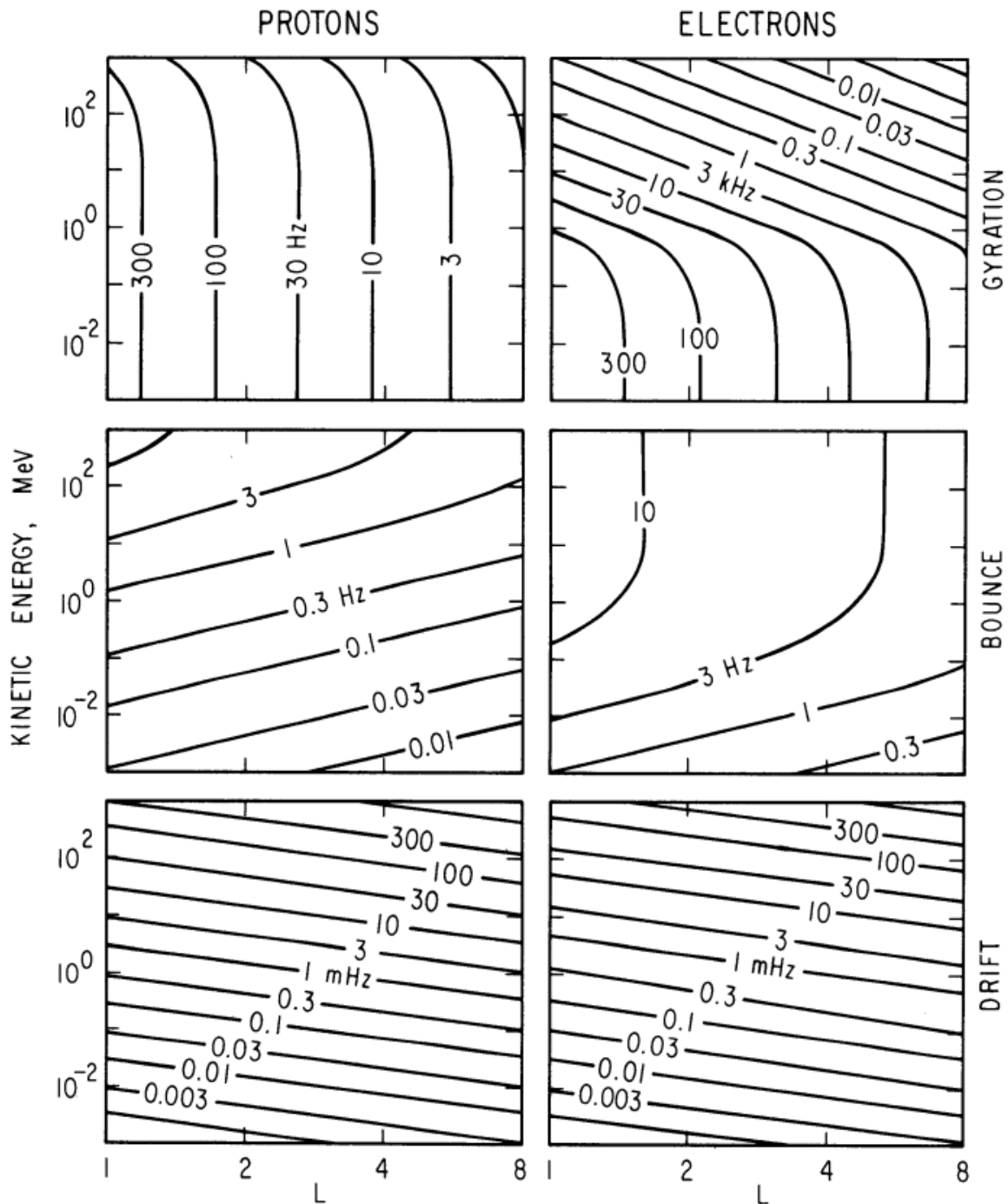


Figure 1.9: Contours of constant gyration, bounce, and drift frequencies for electrons and protons in a dipole field. Figure from Schulz and Lanzerotti (1974).

Radiation Belt Particle Sources and Sinks

Due to the highly energetic and dynamic nature of the radiation belts, and their impact on space exploration, the radiation belts have been studied for over half a century. Researchers have studied and attempted to predict the dynamics of radiation belt particles, waves, and wave-particle interactions by considering various competing particle acceleration and loss mechanisms which are described below.

Adiabatic Heating

One of the particle heating and transport mechanisms arises from the earthward convection of particles. As shown in Eq. 1.5, the conservation of J_1 implies that the initial and final v_\perp depends on the change in the magnetic field magnitude. As a particle convects earthward $B_f > B_i$ and thus v_\perp must also increase. The dipole magnetic field magnitude falls off radially as $B \sim L^{-3}$, and the change in v_\perp^2 as the particle convects towards a stronger magnetic field is

$$\frac{v_{\perp f}^2}{v_{\perp i}^2} = \left(\frac{L_i}{L_f} \right)^3. \quad (1.12)$$

For a particle convecting earthward, if J_2 is conserved, its v_{\parallel} also increases because the distance between the particle's mirror points decreases. Calculating the increase in v_{\parallel} is somewhat difficult and is approximately

$$\frac{v_{\parallel f}^2}{v_{\parallel i}^2} = \left(\frac{L_i}{L_f} \right)^k \quad (1.13)$$

where k ranges from 2 for equatorial pitch angles, $\alpha_{eq} = 0^\circ$, to 2.5 for $\alpha_{eq} = 90^\circ$ (Baumjohann and Treumann, 1997). Since the rate of adiabatic heating is greater in the perpendicular direction than heating in the parallel direction, an initially isotropic

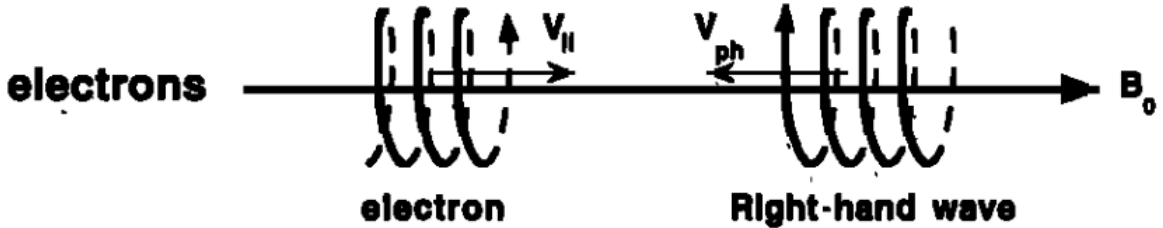
particle distribution will become anisotropic during its convection. These isotropic particles can then become unstable to wave growth and generate waves in order to reach equilibrium.

Wave Resonance Heating

Another mechanism that heats particles is caused by particles resonating with plasma waves. A few of the electromagnetic wave modes responsible for particle acceleration (and scattering) relevant to radiation belt dynamics are hiss, whistler mode chorus (chorus), and electromagnetic ion cyclotron (EMIC) waves. These waves are created by the loss cone instability that is driven by an anisotropy of electrons for chorus waves, and protons for EMIC waves. The level of anisotropy can be quantified by the ratio of the perpendicular to parallel particle temperatures (T_{\perp}/T_{\parallel}). A particle distribution is unstable when $T_{\perp}/T_{\parallel} > 1$. Since electrons gyrate in a right-handed sense, the chorus waves also tend to be right hand circularly polarized (Tsurutani and Lakhina, 1997). The same argument also applies to protons and left hand circularly polarized EMIC waves.

These circularly polarized waves can resonate with electrons and/or protons when their relative motion results in a static \vec{E} in the particle's reference frame. One example of a resonance between a right hand circularly polarized wave and an electron is shown in Fig. 1.10. The electron's v_{\parallel} and the wave's parallel wave vector, k_{\parallel} , are in opposite directions such that the wave frequency, ω , is Doppler shifted to an integer multiple of the Ω_e where the electron feels a static electric field and is accelerated or decelerated. Quantitatively, this resonance condition is easier to understand with the following toy model.

Assume a uniform magnetic field, $\vec{B} = B_0 \hat{z}$, with a parallel propagating ($k = k\hat{z}$), right-hand circularly polarized wave. The wave's electric field as a function of position



$$\omega + \mathbf{k}_{\parallel} \mathbf{v}_{\parallel} = \Omega^-$$

Figure 1.10: The trajectories of an electron and a right-hand circularly polarized wave during a cyclotron resonance. The electron's v_{\parallel} and the wave's k_{\parallel} are in opposite directions such that the wave's frequency is Doppler shifted to an integer multiple of the electron cyclotron frequency. Figure from (Tsurutani and Lakhina, 1997).

and time can be written as

$$\vec{E} = E_0(\cos(\omega t - kz)\hat{x} + \sin(\omega t - kz)\hat{y}). \quad (1.14)$$

The angular component of \vec{E} that will effect the particle's v_{\perp} is

$$E_{\theta} = \vec{E} \cdot \hat{\theta} = E_0 \cos(\omega t - kz + \theta). \quad (1.15)$$

Now assume that the electron is traveling in the $-\hat{z}$ direction with a velocity, $\vec{v} = -v_0\hat{z}$, so its time dependent position along \hat{z} is

$$z(t) = -v_0t \quad (1.16)$$

and gyrophase is

$$\theta(t) = -\Omega t + \theta(0) \quad (1.17)$$

where the first negative sign comes from the electron's negative charge. Now we put

this all together into Eq. 1.1 and find the force that the electron will experience

$$m \frac{dv_\theta}{dt} = qE_\theta = qE_0 \sin((\omega + kv_0 - \Omega)t + \theta(0)). \quad (1.18)$$

This is a relatively complex expression, but when the time dependent component is zero, i.e.

$$\omega + kv_0 - \Omega = 0, \quad (1.19)$$

the electron will feel a static electric field and be accelerated or decelerated depending on $\theta(0)$, the phase between the wave and the electron. The expression in Eq. 1.19 is commonly referred to as the resonance condition and is more generally written as

$$\omega - k_{||}v_{||} = \frac{n\Omega_e}{\gamma} \quad (1.20)$$

where n is the resonance order, and γ is the relativistic correction (e.g. Millan and Thorne, 2007). In the case of the cyclotron resonance ($n = 1$), the wave and cyclotron frequencies are approximately equal and thus J_1 is violated. Since J_1 is violated, J_2 and J_3 are also violated since the conditions required to violate J_2 and J_3 are less stringent than J_1 .

It is important to remember that a particle will experience the effects of many waves along its drift orbit. The typical MLT extent of a handful of waves that are capable of resonating with radiation belt electrons are shown in Fig. 1.11.

Particle Losses

Now that we have seen two general mechanisms with which particles are accelerated in the magnetosphere, we will consider a few specific mechanisms that remove particles from the magnetosphere into the atmosphere or the solar wind.

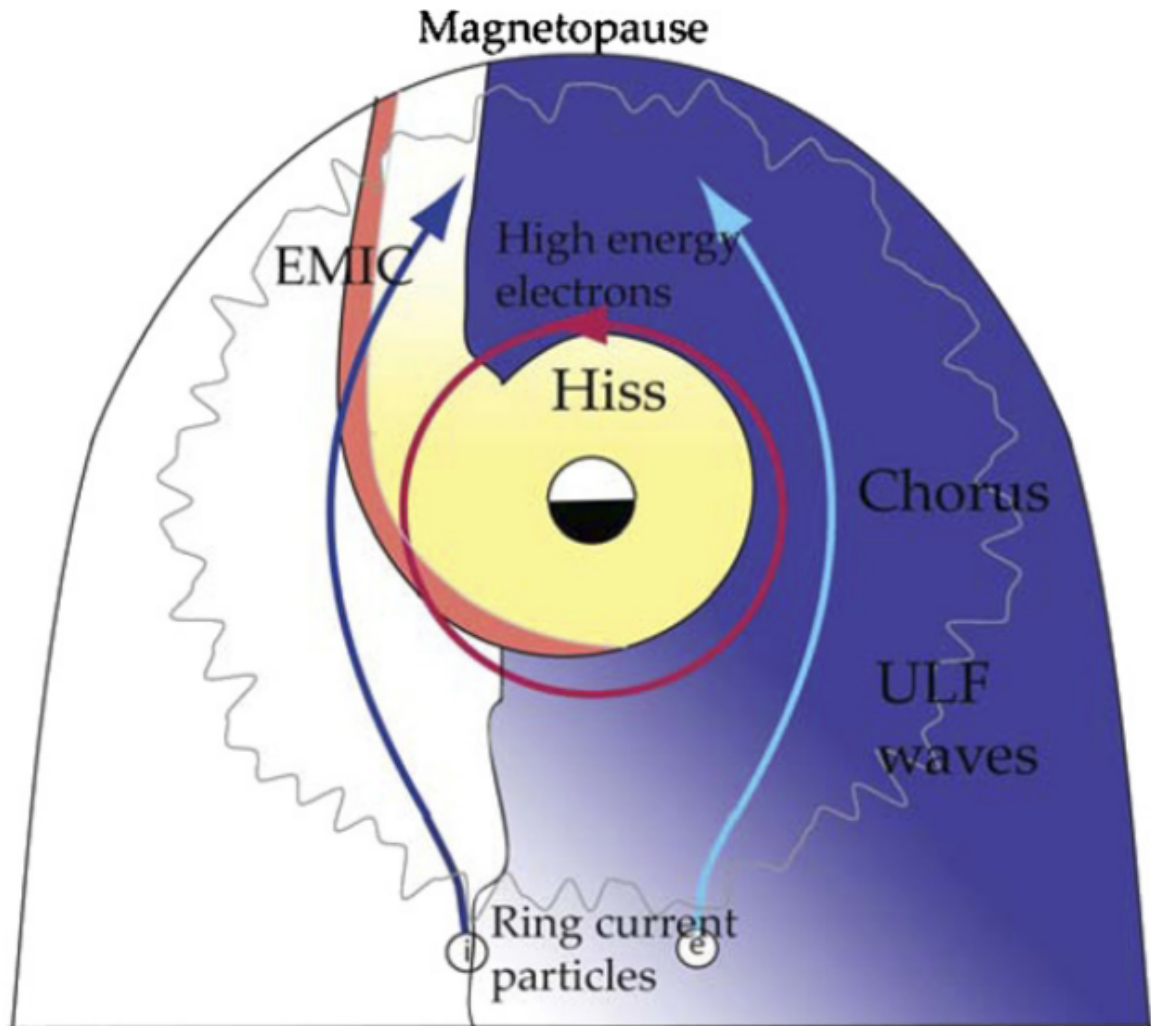


Figure 1.11: Various wave modes in the magnetosphere. Ultra low frequency waves occur through the magnetosphere. Chorus waves are typically observed in the 0-12 midnight-dawn region. EMIC waves are typically observed in the dusk MLT sector. Hiss waves are observed inside the plasmasphere. Figure from Millan and Thorne (2007).

One mechanism that transports magnetosperic particles into the solar wind is magnetopause shadowing (e.g. Ukhorskiy et al., 2006). Magnetopause shadowing occurs when the ring current is strengthened and Earth's magnetic field strength is increased outside of the ring current. If the ring current increases slowly enough (such that J_3 is conserved), a particle drift shell will move outward to conserve J_3 . If the particle's drift shell expands past the magnetopause, the particle will be lost to the solar wind.

Another particle loss (and acceleration) mechanism is called radial diffusion and is driven by ultra low frequency (ULF) modulation of Earth's magnetic field. For example, if the solar wind compresses the magnetopause on time scales shorter than the drift period, particles will experience radial diffusion. If the transport is radially inward, particles will be accelerated. On the other hand, radially outward radial diffusion can transport particles through the magnetopause where they will be lost to the solar wind. Reeves et al. (2013) investigated the driver of particle acceleration during the October 2012 storm and observationally found that inward radial diffusion was not dominant, rather local acceleration via wave-resonance heating appeared to be the dominant acceleration mechanism.

The loss mechanism central to this dissertation is pitch angle and energy scattering of electrons by waves. Some of the waves that scatter electrons in energy and pitch angle in the inner magnetosphere are: plasmaspheric hiss (e.g. Breneman et al., 2015; O'Brien et al., 2014), EMIC waves (e.g. Capannolo et al., 2019; Hendry et al., 2017), and chorus waves (e.g. Breneman et al., 2017; Kasahara et al., 2018; Ozaki et al., 2019). These wave-particle interactions occur when the resonance condition in Eq. 1.20 is satisfied and the particle's energy and α is modified by the wave. More details regarding the theory of pitch angle and energy diffusion is given in Chapter ???. If the wave changes α towards zero and $\alpha < \alpha_L$, then the

particle's mirror point dips below 100 km altitude where the particle can be lost from the magnetosphere. One manifestation of pitch angle scattering of particles into the loss cone are microbursts, a sub-second duration impulse of electrons.

Microbursts

Microbursts were first seen with high altitude balloons which measured bremsstrahlung X-rays emitted by microburst electrons impacting the atmosphere by Anderson and Milton (1964). In the following years, numerous balloon flights expanded our knowledge of non-relativistic (< 500 keV) microbursts by quantifying the microburst spatial extent, temporal width, occurrence frequency, extent in L and MLT, and their source. It is worth noting that relativistic microbursts have not yet been observed by high altitude balloons. The microburst source was initially believed to be either a local plasma instability or a propagating disturbance in the magnetosphere (Barcus et al., 1966; Parks, 1967; Trefall et al., 1966; ?). Soon after, both non-relativistic and relativistic microburst electrons were directly observed in LEO with spacecraft including the Solar Anomalous and Magnetospheric Particle Explorer (SAMPEX) (e.g. Blake et al., 1996; Blum et al., 2015; Douma et al., 2017; Greeley et al., 2019; Lorentzen et al., 2001a,b; Nakamura et al., 1995, 2000; O'Brien et al., 2004, 2003; ?), Montana State University's (MSU) Focused Investigation of Relativistic Electron Bursts: Intensity, Range, and Dynamics II (FIREBIRD-II) (Anderson et al., 2017; Breneman et al., 2017; Crew et al., 2016; ?; ?), and Science Technologies Satellite (STSAT-I) (e.g. Lee et al., 2012, 2005). An example microburst time series observed by the FIREBIRD-II CubeSats is shown in Fig. 1.12. The prominent features of the example microbursts in Fig. 1.12 are their sub-second duration, half order of magnitude increase in count rate above the falling background, and their 200-800 keV energy extent.

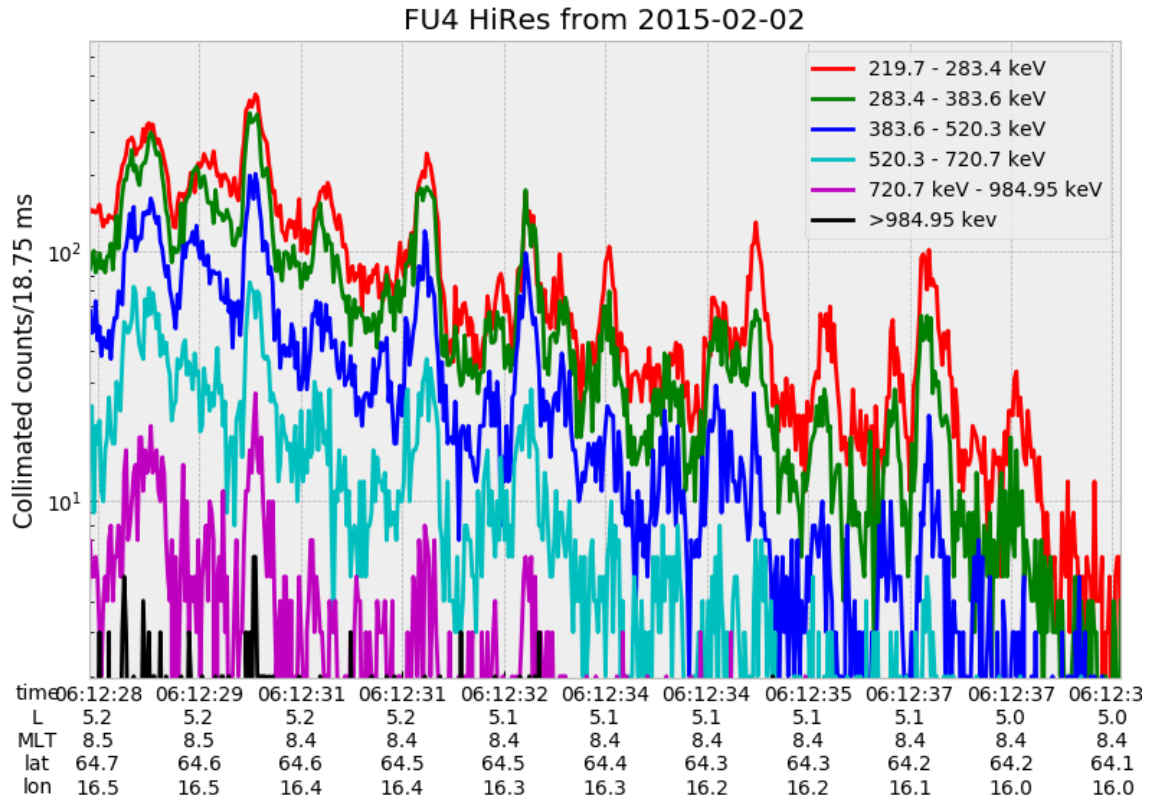


Figure 1.12: An example train of microbursts observed by FIREBIRD-II unit 4 on February 2nd, 2015. The colored curves show the differential energy channel count rates in five channels from ≈ 200 keV to 1 MeV and a sixth integral energy channel with a 1 MeV threshold. The x-axis labels show auxiliary information such as time of observation and the spacecraft position in L, MLT, latitude and longitude coordinates.

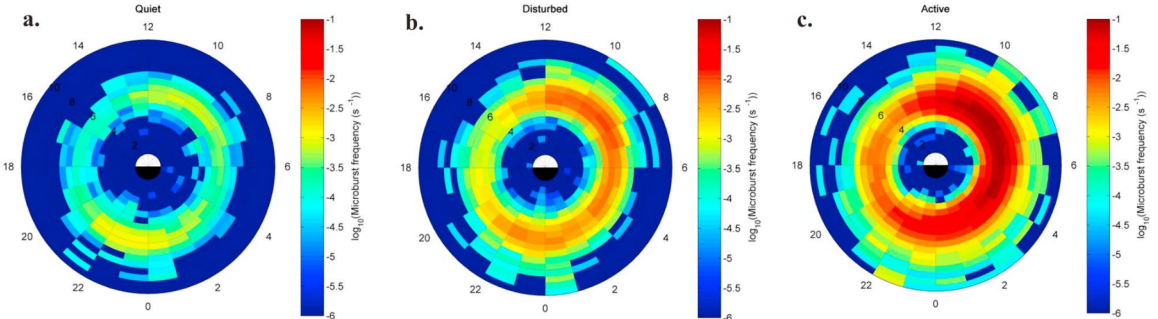


Figure 1.13: Distribution of > 1 MeV microburst occurrence rates as a function of L and MLT. The three panels show the microburst occurrence rate dependence on geomagnetic activity, parameterized by the auroral electrojet (AE) index for (a) $\text{AE} < 100$ nT, (b) $100 < \text{AE} < 300$ nT and (c) $\text{AE} > 300$ nT. Figure from Douma et al. (2017).

Microbursts are observed on magnetic field footprints that are connected to the outer radiation belt (approximately $4 < L < 8$). They are predominately observed in the 0-12 MLT sector with an elevated occurrence frequency during magnetospherically disturbed times as shown in Fig. 1.13. O'Brien et al. (2003) used SAMPEX relativistic electron data and found that microbursts predominately occur during the main phase of storms, with a heightened occurrence rate during the recovery phase. Microburst occurrence rates are also higher during high solar wind velocity events e.g. from co-rotating interaction regions (Greeley et al., 2019; O'Brien et al., 2003).

The estimated impact of microbursts on the atmosphere and the radiation belts is significant. Relativistic microburst electrons impacting the atmosphere are ionized at < 100 km altitudes, with higher energy electrons penetrating closer to the surface. The resulting chemical reaction of microburst electrons impacting the atmosphere produces odd hydrogen HO_x and odd nitrogen NO_x molecules, which are partially responsible for destroying ozone (O_3). ? modeled a six hour relativistic microburst storm and found that the mesospheric ozone was reduced by 7 – 12% in the summer months and 12 – 20% in the winter months, so microbursts may have a non-negligible

contribution to the dynamics of atmospheric ozone. Furthermore, microbursts have also been estimated to have a significant impact on the outer radiation belt electron population. The loss of all radiation belt electrons due to microbursts have been estimated to be on the order of a day (Breneman et al., 2017; Lorentzen et al., 2001b; O'Brien et al., 2004; ?; ?).

The wave-particle interactions responsible for generating microbursts are also believed to accelerate electrons in the radiation belts. As mentioned earlier, when an electron is in resonance with a wave, energy is exchanged with the wave and the electron is either accelerated or decelerated. The signature of wave-particle acceleration been observed for radiation belt electrons (e.g. Horne et al., 2005; Reeves et al., 2013; ?), and O'Brien et al. (2003) presented evidence that enhancements in chorus waves, microbursts, and radiation belt electrons are related. To explain their observations, O'Brien et al. (2003) proposed that microburst precipitation is a side effect of electron acceleration due to chorus waves.

The widely used theoretical framework to model the wave-particle interactions responsible for accelerating electrons and scattering microbursts is quasi-linear diffusion (e.g. Horne et al., 2005; ?; ?; ?; ?; ?). This framework is explained in Chapter ??, and applied to an observation of a microburst in the heart of the radiation belt. Qualitatively, when a particle is resonant with a wave it can either be transported in pitch angle towards the loss cone and lose energy to the wave, or transported away from the loss cone and gain energy from the wave.

As previously mentioned, the range of observed microburst energies range from a few tens of keV (e.g Datta et al., 1997; Parks, 1967) to greater than 1 MeV (e.g. Blake et al., 1996; Greeley et al., 2019). The microburst electron flux (J) falls off in energy,

and the microburst energy spectra is typically well fit to a decaying exponential

$$J(E) = J_0 e^{-E/E_0} \quad (1.21)$$

where J_0 is the flux at 0 keV (unphysical free parameter) and E_0 quantifies the efficiency of the scattering mechanism in energy (e.g. Datta et al., 1997; Lee et al., 2005; Parks, 1967). A small E_0 suggests that mostly low energy particles are scattered. In contrast a high E_0 suggests that the scattering mechanism scatters low and high energy electrons. Reality is a bit more messy and a high E_0 may be a signature of a scattering mechanism that is most efficient at scattering high energy electrons, with a relatively minor efficiency to scatter low energy electrons. Since there are many more low energy electrons available to scatter, there may be relatively more low energy electrons scattered.

The short microburst duration, as observed by a single LEO satellite in a highly inclined orbit (motion is mostly latitudinal), has an ambiguity when interpreting what is a microburst. The two possible realities are: a microburst is very narrow in latitude and persistent, or transient. There are a few ways to distinguish between the two possible realities, and each one has a unique set of advantages.

A high altitude balloon essentially provides a stationary view of the precipitating particles under the radiation belt footprints. An intense transient microburst can be unambiguously identified above the slowly varying background. On the other hand, if the microburst precipitation is stationary, there will be too little contrast between the microburst and the background fluxes to be found.

Multi-spacecraft missions provide an alternate solution that can determine if a microburst is a spatial or a transient phenomena. As is illustrated in Fig. 1.14, a transient microburst can be recognized if two spacecraft, one trailing the other,

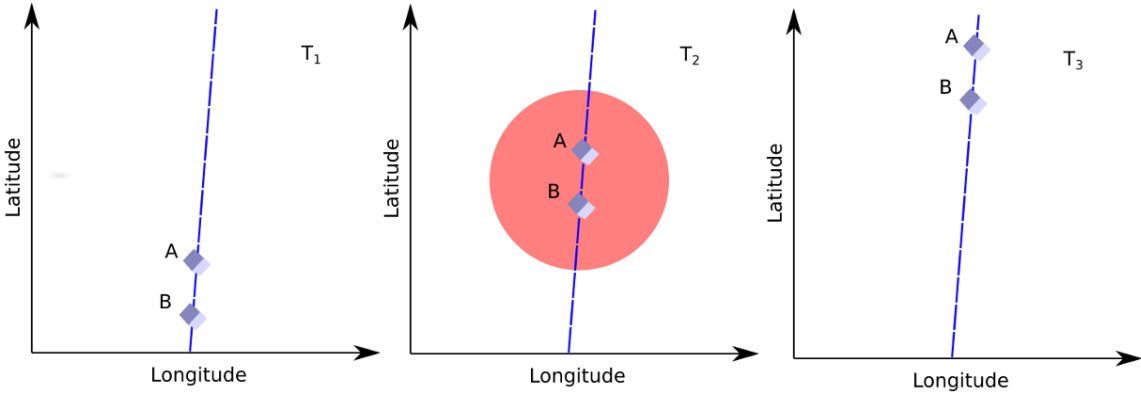


Figure 1.14: Three snapshots of a temporal microburst observed simultaneously by a pair of polar-orbiting spacecraft. The spacecraft are identified by labels "A" and "B" and are traveling upwards on the blue dashed orbital track. At T_1 the spacecraft are traveling upwards and no microburst is observed. Then at T_2 both spacecraft simultaneously observe a microburst shown by the red circle and the microburst size must be greater than the spacecraft separation. In the last snapshot, T_3 , the microburst has precipitated and no longer observed by the spacecraft.

simultaneously observe it. The size of the microburst footprint must then be larger than the spacecraft separation. On the contrary, if two spacecraft observe a microburst-like feature at the same location but at different times, then the spatially stationary and latitudinally small feature may be a curtain (Blake and O'Brien, 2016). Both balloon and multi-spacecraft observational methods have a unique set of strengths. This dissertation takes the multi-spacecraft approach to identify and study microbursts.

Scope of Research

This dissertation furthers our understanding of the microburst scattering mechanism by presenting observational evidence of microburst scattering directly, and measuring microburst sizes and comparing them to the size of chorus waves. Chapter ?? describes a microburst scattering event observed by NASA's Van Allen

Probes. For this event, particle and wave measurements were analyzed and modeled in the theoretical framework of pitch angle and energy diffusion. The following two chapters present studies of microburst sizes in comparison to chorus waves. Chapter ?? describes a bouncing packet microburst observation made by the FIREBIRD-II mission where the microburst's lower bound longitudinal and latitudinal sizes were estimated. Chapter ?? expands the case study from Chapter ?? to a statistical study of microburst sizes using The Aerospace Corporation's AeroCube-6 (AC6) CubeSats. In this study, a Monte Carlo and analytic microburst size models were developed to account for the compounding statistical effects of random microburst sizes and locations. Lastly, Chapter ?? will summarize this work and make concluding remarks regarding outstanding questions in microburst physics.

REFERENCES CITED

Bibliography

- Anderson, B., Shekhar, S., Millan, R., Crew, A., Spence, H., Klumpar, D., Blake, J., O'Brien, T., and Turner, D. (2017). Spatial scale and duration of one microburst region on 13 August 2015. *Journal of Geophysical Research: Space Physics*.
- Anderson, K. A. and Milton, D. W. (1964). Balloon observations of X rays in the auroral zone: 3. High time resolution studies. *Journal of Geophysical Research*, 69(21):4457–4479.
- Barcus, J., Brown, R., and Rosenberg, T. (1966). Spatial and temporal character of fast variations in auroral-zone x rays. *Journal of Geophysical Research*, 71(1):125–141.
- Baumjohann, W. and Treumann, R. A. (1997). *Basic space plasma physics*. World Scientific.
- Blake, J.,Looper, M., Baker, D., Nakamura, R., Klecker, B., and Hovestadt, D. (1996). New high temporal and spatial resolution measurements by sampex of the precipitation of relativistic electrons. *Advances in Space Research*, 18(8):171 – 186.
- Blake, J. B. and O'Brien, T. P. (2016). Observations of small-scale latitudinal structure in energetic electron precipitation. *Journal of Geophysical Research: Space Physics*, 121(4):3031–3035. 2015JA021815.
- Blum, L., Li, X., and Denton, M. (2015). Rapid MeV electron precipitation as observed by SAMPEX/HILT during high-speed stream-driven storms. *Journal of Geophysical Research: Space Physics*, 120(5):3783–3794. 2014JA020633.
- Breneman, A., Crew, A., Sample, J., Klumpar, D., Johnson, A., Agapitov, O., Shumko, M., Turner, D., Santolik, O., Wygant, J., et al. (2017). Observations directly linking relativistic electron microbursts to whistler mode chorus: Van allen probes and FIREBIRD II. *Geophysical Research Letters*.
- Breneman, A. W., Halford, A., Millan, R., McCarthy, M., Fennell, J., Sample, J., Woodger, L., Hospodarsky, G., Wygant, J. R., Cattell, C. A., et al. (2015). Global-scale coherence modulation of radiation-belt electron loss from plasmaspheric hiss. *Nature*, 523(7559):193.
- Brown, R., Barcus, J., and Parsons, N. (1965). Balloon observations of auroral zone x rays in conjugate regions. 2. microbursts and pulsations. *Journal of Geophysical Research (U.S.)*.
- Capannolo, L., Li, W., Ma, Q., Shen, X.-C., Zhang, X.-J., Redmon, R., Rodriguez, J., Engebretson, M., Kletzing, C., Kurth, W., et al. (2019). Energetic electron precipitation: multi-event analysis of its spatial extent during emic wave activity. *Journal of Geophysical Research: Space Physics*.

- Claudepierre, S., O'Brien, T., Looper, M., Blake, J., Fennell, J., Roeder, J., Clemmons, J., Mazur, J., Turner, D., Reeves, G., et al. (2019). A revised look at relativistic electrons in the earth's inner radiation zone and slot region. *Journal of Geophysical Research: Space Physics*, 124(2):934–951.
- Crew, A. B., Spence, H. E., Blake, J. B., Klumpar, D. M., Larsen, B. A., O'Brien, T. P., Driscoll, S., Handley, M., Legere, J., Longworth, S., Mashburn, K., Mosleh, E., Ryhajlo, N., Smith, S., Springer, L., and Widholm, M. (2016). First multipoint in situ observations of electron microbursts: Initial results from the NSF FIREBIRD II mission. *Journal of Geophysical Research: Space Physics*, 121(6):5272–5283. 2016JA022485.
- Datta, S., Skoug, R., McCarthy, M., and Parks, G. (1997). Modeling of microburst electron precipitation using pitch angle diffusion theory. *Journal of Geophysical Research: Space Physics*, 102(A8):17325–17333.
- Douma, E., Rodger, C. J., Blum, L. W., and Clilverd, M. A. (2017). Occurrence characteristics of relativistic electron microbursts from SAMPEX observations. *Journal of Geophysical Research: Space Physics*, 122(8):8096–8107. 2017JA024067.
- Dungey, J. W. (1961). Interplanetary magnetic field and the auroral zones. *Phys. Rev. Lett.*, 6:47–48.
- Greeley, A., Kanekal, S., Baker, D., Klecker, B., and Schiller, Q. (2019). Quantifying the contribution of microbursts to global electron loss in the radiation belts. *Journal of Geophysical Research: Space Physics*.
- Hendry, A. T., Rodger, C. J., and Clilverd, M. A. (2017). Evidence of sub-mev emic-driven electron precipitation. *Geophysical Research Letters*, 44(3):1210–1218.
- Horne, R., Glauert, S., Meredith, N., Boscher, D., Maget, V., Heynderickx, D., and Pitchford, D. (2013). Space weather impacts on satellites and forecasting the earth's electron radiation belts with spacecast. *Space Weather*, 11(4):169–186.
- Horne, R. B., Thorne, R. M., Shprits, Y. Y., Meredith, N. P., Glauert, S. A., Smith, A. J., Kanekal, S. G., Baker, D. N., Engebretson, M. J., Posch, J. L., et al. (2005). Wave acceleration of electrons in the van allen radiation belts. *Nature*, 437(7056):227.
- Kasahara, S., Miyoshi, Y., Yokota, S., Mitani, T., Kasahara, Y., Matsuda, S., Kumamoto, A., Matsuoka, A., Kazama, Y., Frey, H., et al. (2018). Pulsating aurora from electron scattering by chorus waves. *Nature*, 554(7692):337.
- Lee, J. J., Parks, G. K., Lee, E., Tsurutani, B. T., Hwang, J., Cho, K. S., Kim, K.-H., Park, Y. D., Min, K. W., and McCarthy, M. P. (2012). Anisotropic pitch angle distribution of 100 keV microburst electrons in the loss cone: measurements from STSAT-1. *Annales Geophysicae*, 30(11):1567–1573.

- Lee, J.-J., Parks, G. K., Min, K. W., Kim, H. J., Park, J., Hwang, J., McCarthy, M. P., Lee, E., Ryu, K. S., Lim, J. T., Sim, E. S., Lee, H. W., Kang, K. I., and Park, H. Y. (2005). Energy spectra of 170–360 keV electron microbursts measured by the korean STSAT-1. *Geophysical Research Letters*, 32(13). L13106.
- Li, X., Selesnick, R., Schiller, Q., Zhang, K., Zhao, H., Baker, D. N., and Temerin, M. A. (2017). Measurement of electrons from albedo neutron decay and neutron density in near-earth space. *Nature*, 552(7685):382.
- Lorentzen, K. R., Blake, J. B., Inan, U. S., and Bortnik, J. (2001a). Observations of relativistic electron microbursts in association with VLF chorus. *Journal of Geophysical Research: Space Physics*, 106(A4):6017–6027.
- Lorentzen, K. R.,Looper, M. D., and Blake, J. B. (2001b). Relativistic electron microbursts during the GEM storms. *Geophysical Research Letters*, 28(13):2573–2576.
- Lyons, L. R. and Thorne, R. M. (1973). Equilibrium structure of radiation belt electrons. *Journal of Geophysical Research*, 78(13):2142–2149.
- Millan, R. and Thorne, R. (2007). Review of radiation belt relativistic electron losses. *Journal of Atmospheric and Solar-Terrestrial Physics*, 69(3):362 – 377.
- Nakamura, R., Baker, D. N., Blake, J. B., Kanekal, S., Klecker, B., and Hovestadt, D. (1995). Relativistic electron precipitation enhancements near the outer edge of the radiation belt. *Geophysical Research Letters*, 22(9):1129–1132.
- Nakamura, R., Isowa, M., Kamide, Y., Baker, D., Blake, J., and Looper, M. (2000). Observations of relativistic electron microbursts in association with VLF chorus. *J. Geophys. Res.*, 105:15875–15885.
- O'Brien, T., Claudepierre, S., Blake, J., Fennell, J. F., Clemons, J., Roeder, J., Spence, H. E., Reeves, G., and Baker, D. (2014). An empirically observed pitch-angle diffusion eigenmode in the earth's electron belt near $l^*= 5.0$. *Geophysical Research Letters*, 41(2):251–258.
- O'Brien, T., Claudepierre, S., Guild, T., Fennell, J., Turner, D., Blake, J., Clemons, J., and Roeder, J. (2016). Inner zone and slot electron radial diffusion revisited. *Geophysical Research Letters*, 43(14):7301–7310.
- O'Brien, T. and Moldwin, M. (2003). Empirical plasmapause models from magnetic indices. *Geophysical Research Letters*, 30(4).
- O'Brien, T. P., Looper, M. D., and Blake, J. B. (2004). Quantification of relativistic electron microburst losses during the GEM storms. *Geophysical Research Letters*, 31(4). L04802.

- O'Brien, T. P., Lorentzen, K. R., Mann, I. R., Meredith, N. P., Blake, J. B., Fennell, J. F., Looper, M. D., Milling, D. K., and Anderson, R. R. (2003). Energization of relativistic electrons in the presence of ULF power and MeV microbursts: Evidence for dual ULF and VLF acceleration. *Journal of Geophysical Research: Space Physics*, 108(A8).
- Ozaki, M., Miyoshi, Y., Shiokawa, K., Hosokawa, K., Oyama, S.-i., Kataoka, R., Ebihara, Y., Ogawa, Y., Kasahara, Y., Yagitani, S., et al. (2019). Visualization of rapid electron precipitation via chorus element wave-particle interactions. *Nature communications*, 10(1):257.
- Parks, G. K. (1967). Spatial characteristics of auroral-zone X-ray microbursts. *Journal of Geophysical Research*, 72(1):215–226.
- Reeves, G., Spence, H. E., Henderson, M., Morley, S., Friedel, R., Funsten, H., Baker, D., Kanekal, S., Blake, J., Fennell, J., et al. (2013). Electron acceleration in the heart of the van allen radiation belts. *Science*, 341(6149):991–994.
- Reeves, G. D., McAdams, K. L., Friedel, R. H. W., and O'Brien, T. P. (2003). Acceleration and loss of relativistic electrons during geomagnetic storms. *Geophysical Research Letters*, 30(10):n/a–n/a. 1529.
- Schulz, M. and Lanzerotti, L. J. (1974). *Particle Diffusion in the Radiation Belts*. Springer.
- Trefall, H., Bjordal, J., Ullaland, S., and Stadsnes, J. (1966). On the extension of auroral-zone x-ray microbursts. *Journal of Atmospheric and Terrestrial Physics*, 28(2):225–233.
- Tsurutani, B. T. and Lakhina, G. S. (1997). Some basic concepts of wave-particle interactions in collisionless plasmas. *Reviews of Geophysics*, 35(4):491–501.
- Turner, D., Claudepierre, S., Fennell, J., O'Brien, T., Blake, J., Lemon, C., Gkioulidou, M., Takahashi, K., Reeves, G., Thaller, S., et al. (2015). Energetic electron injections deep into the inner magnetosphere associated with substorm activity. *Geophysical Research Letters*, 42(7):2079–2087.
- Ukhorskiy, A. Y., Anderson, B. J., Brandt, P. C., and Tsyganenko, N. A. (2006). Storm time evolution of the outer radiation belt: Transport and losses. *Journal of Geophysical Research: Space Physics*, 111(A11):n/a–n/a. A11S03.
- Van Allen, J. A. (1959). The geomagnetically trapped corpuscular radiation. *Journal of Geophysical Research*, 64(11):1683–1689.
- Vernov, S. and Chudakov, A. (1960). Investigation of radiation in outer space. In *International Cosmic Ray Conference*, volume 3, page 19.

Woodger, L., Halford, A., Millan, R., McCarthy, M., Smith, D., Bowers, G., Sample, J., Anderson, B., and Liang, X. (2015). A summary of the BARREL campaigns: Technique for studying electron precipitation. *Journal of Geophysical Research: Space Physics*, 120(6):4922–4935.